# A Study of Energy Losses in the World's Most Fuel-Efficient Vehicle

Patrick Grady*, Gerry Chen*, Shomik Verma†, Aniruddh Marellapudi‡, Nico Hotz†
*Electrical and Computer Engineering
†Mechanical Engineering and Material Science
‡Biomedical Engineering
Duke University, Durham, NC, USA
Email: patrick.grady@gatech.edu

***Abstract*—The prototype fuel cell electric vehicle (FCEV) Maxwell currently holds the Guinness World Record for "Most Fuel-Efficient Vehicle" at 6,196 km/l (14,573 MPGe). The vehicle draws less than 21W of electrical power at 25 km/h. This work outlines the powertrain architecture and presents the vehicle's sources of electrical and mechanical losses, quantified through rigorous experimentation. The individual components are modelled and combined into a total model of performance representing all energy flow in the vehicle. The total model is found to have excellent predictive power with only 4.3% error compared to measured on-track performance.**

***Index Terms*—efficiency, fuel cell vehicle, electric vehicle, eco-marathon, correlation, world record, motor characterization**

## I. Introduction

While commercial passenger vehicles, designed around safety, comfort, and reliability, have efficiencies in the range of 8-22 km/l (20-50 MPG) [1], "supermileage" vehicles, designed with the singular goal of consuming as little fuel as possible to travel a fixed distance, have efficiencies in the 1000s of km/l [2]. Due to their extreme designs, supermileage vehicles have the highest efficiencies of all land vehicles.

The development of supermileage vehicles is facilitated through multiple international competitions such as SAE Supermileage, EducEco, and the Shell Eco-Marathon. In these events, student teams compete to build the most efficient prototype. The vehicle that uses the least amount of fuel to travel a fixed distance around a track is declared the winner. To establish a baseline of fairness, the competition mandates constraints such as minimum driver weight and minimum average speed. The vehicles must also comply with rules designed to ensure the safety of the competition, such as minimum vehicle track width and driver protection [3].

In 2017, the Duke Electric Vehicles team designed and built Maxwell, originally a battery-electric vehicle. Maxwell competed in the 2017 Shell Eco-Marathon Americas, winning against 27 other teams. It competed again in the 2018 Eco-Marathon with minimal modifications, again taking first place. [2]. During the summer of 2018, the vehicle was extensively modified and converted into a FCEV to attempt to break the Guinness World Record for "Most Fuel-Efficient Vehicle".

This work was supported by grants from the Lord Foundation, General Motors, the Duke Engineering Alumni Council, and the North Carolina Space Grant.

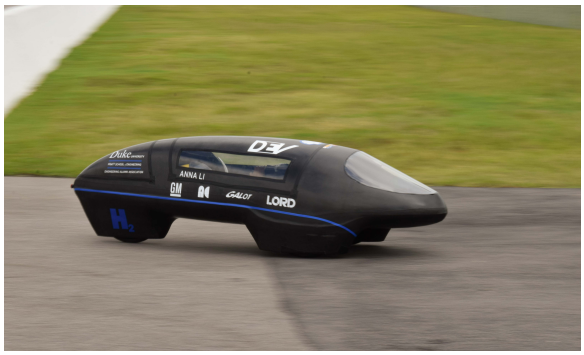


Fig. 1: Maxwell during the world record attempt

The previous world record was set in 2005 at 5,385 km/l by the PAC CAR II, a FCEV built by ETH Zurich. Due to the vehicle's excellent optimization and design, the record stood for 13 years.

In July 2018, Maxwell successfully broke the Guinness World Record for "Most Fuel-Efficient Vehicle," achieving 6,196 km/l of gasoline equivalent (14,573 MPGe) [4]. For perspective, this is more than 500x the efficiency of the average passenger vehicle [1] and roughly 2x the efficiency of top-performing Eco-Marathon vehicles [2].

This paper individually analyzes each source of loss in the vehicle in a bottom-up approach. The losses are first modeled, and then combined to determine the overall energy flow for the vehicle. The overall model is then correlated with the actual vehicle's on-track performance, and excellent agreement is observed. Previous works, notably [5], have characterized individual sources of losses in supermileage vehicles, but the authors consider the current work novel in combining all sources of losses to generate an overall model, thus building a complete understanding of such vehicles. The modelling effort was critical to the success of the vehicle as it allowed the team to effectively prioritize improvements.

Although this paper is written to specifically describe Maxwell in its world record configuration, the insights gained are easily applicable to all supermileage and efficient vehicles, and many of the novel testing methods can be applied more broadly. This work attempts to generate a model that strikes a

balance between accuracy, flexibility, and simplicity in order to maximize its utility in optimizing vehicle efficiency. In this vein, the considerations of a FCEV are broadly separated into fuel cell (FC) architecture, motor losses, and mechanical losses.

## II. Fuel Cell Architecture

Maxwell was powered by a proton exchange membrane (PEM) FC. Compared to normal passenger FCEVs, supermileage vehicles' power demands are so low that atypical fuel cell architectures may be considered. While larger FCEVs typically have recirculation pumps and/or active humidification systems [6]–[8], implementing these fuel cell auxiliaries in supermileage vehicles would consume a significant percentage of total power. Thus, a simple fuel cell with a dead-ended anode and passive humidification was selected. This architecture has higher peak efficiency but suffers from increased sensitivity to load and environmental variables (temperature, humidity, etc.) [9]–[11].

PEM FCs have a maximum theoretical thermal efficiency of 82.7% [12]. However, typical real world efficiencies range from 40-60% [13]. In fuel cells, most losses are due to crossover loss, activation loss, ohmic loss, and mass transfer loss, but additional losses exist due to fuel cell regulation and control. Short circuiting and purging are used to regulate humidity [11], a fan is needed to prevent oxygen starvation and limit temperature [14], and associated control electronics are required which draw power.

A Horizon H-100 fuel cell was selected for the vehicle's energy source. Its performance is characterized in Figure 2 and quantified by the empirical equations:

$$\eta_{FC} = \frac{P_{eFC}}{P_{eFC} + P_l} \tag{1}$$

$$P_l(P_{eFC}) = 0.26 + 0.56P_{eFC} + 0.0047P_{eFC}^2 \tag{2}$$

where $\eta_{FC}$ is fuel cell efficiency, $P_l$ is the power lost by the fuel cell, and $P_{eFC}$ is fuel cell output power. While this is a valuable reference curve, the authors note that efficiency may change by up to 3% depending on environmental conditions.

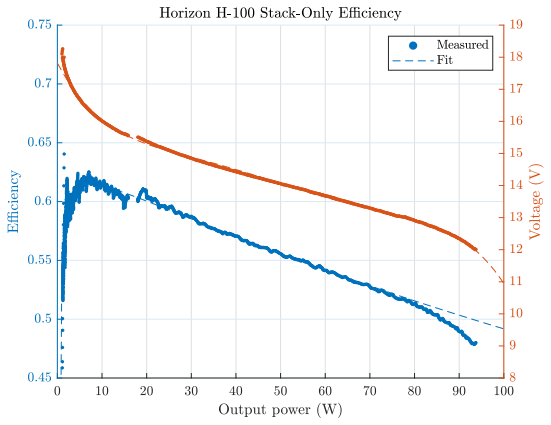


Fig. 2: Horizon H-100 fuel cell measured efficiency

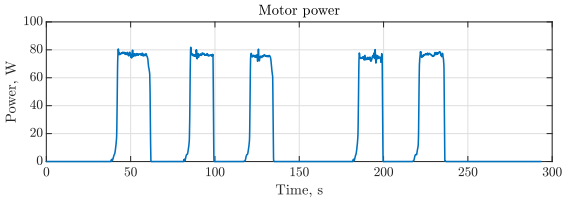


Fig. 3: Demanded power over one lap from the world record attempt

During the official world record attempt, the overall fuel cell system efficiency, including all auxiliary losses, was measured to be 58.4%.

### A. Load-Levelling

Due to the elevation change of the track and the efficiency characteristics of the motor, the motor was used in a "pulse and glide" strategy, depicted in Figure 3. Passing this pulsed load directly to the fuel cell would be undesirable as this would poorly match the fuel cell efficiency curve (see Figure 2) and would require robustness to dynamic load. Instead, load-levelling solutions were considered to allow the fuel cell to operate at a more constant power level. Three solutions were compared: the simple solution with no load-levelling, a passive load-levelling solution with a large supercapacitor (SC) module, and an active solution with a DC/DC converter and a smaller SC module, shown in Figure 4. They are compared in Table I. Note that supercapacitors were selected for their low internal resistance per unit mass, as opposed to more commonly used lithium batteries.

The passive supercapacitor load-levelling system was selected due to its high system efficiency. Additionally, the simplicity and robustness of the passive solution were attractive in developing a reliable vehicle.

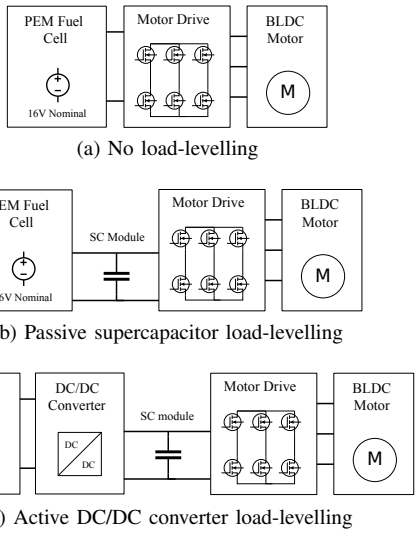


(a) No load-levelling

(b) Passive supercapacitor load-levelling

(c) Active DC/DC converter load-levelling

Fig. 4: Load-levelling fuel cell architectures

TABLE I: Load-levelling (LL) comparison

| | No LL | Passive LL | Active LL |
|---|---|---|---|
| Energy storage | None | SC, 170F | SC, 40F |
| Mass | 0kg | 2.2kg | 0.8kg |
| FC power range | 0-77W | 14W-27W | 21W |
| FC eff. | 51.7% | 59.8% | 60.0% |
| FC aux. loss | 1.4% | 1.4% | 1.4% |
| SC loss | 0% | 0.2% | 0.8% |
| DC/DC loss | 0% | 0% | 3% |
| **System eff.** | **51.0%** | **58.9%** | **56.9%** |

## III. Traction Motor Losses

Due to the low motor power required by the vehicle (21W on average), as well as the dynamic torque requirements inherent to vehicle propulsion, a brushless DC (BLDC) motor was selected. Important design constraints included minimum weight, efficient operation at low powers, and a low motor velocity constant ($K_v$). As transmission losses generally increase with larger speed ratios, a low $K_v$ allowed power delivery to the wheel using a single stage chain drive.

Several competing BLDC motors were characterized to determine real-world motor performance and to formulate an empirical model of motor losses. For this purpose, a custom inertial dynamometer, featuring a similar chain transmission as the vehicle, was constructed. The resulting data exhibited high repeatability (on the order of 1%). Figure 5 depicts representative results of dynamometer testing with five trials overlayed on each other. Ultimately, the Koford 60LH175 motor [15] was chosen, with a measured peak efficiency of 88%.

The first pass motor-chain loss model considers only three loss mechanisms: copper, controller, and no-load losses. Copper losses are given by $P_\Omega = I^2 R_s$, controller losses by a quiescent $P_Q$, and combined no-load losses by $P_n(\omega)$ – a third degree polynomial of angular velocity, $\omega$. $I$ denotes DC current and $R_s$ denotes phase-phase winding resistance. The efficiency of the motor-chain system is then given by:

$$\eta_m = 1 - \frac{I^2 R_s + P_Q + P_n(\omega)}{P_e} \tag{3}$$

where $P_e$ denotes the total electrical input power to the motor.

Additionally, the DC current, DC voltage, and speed can be related by the winding constant and parameters in the equation:

$$V - \frac{\omega}{K_v} = I\sqrt{R_s^2 + (\omega L_s)^2} \tag{4}$$

where $L_s$ denotes the phase-phase winding inductance.

The model (shown as "motor model 1" in Figure 5) is remarkably accurate, while also consisting purely of parameters which are easy to measure. $R_s$ and $L_s$ were taken from the manufacturer datasheet and $P_Q$ was measured directly from the controller with phase wires disconnected. The no-load losses were measured by driving the motor without any load attached at a sweep of speeds and calculating power loss as electrical power less the modelled copper and controller losses and fit to a third degree polynomial as a function of $\omega$. Note that the winding resistance, $R_s$, and inductance, $L_s$, were manually tuned to better match the empirical data.

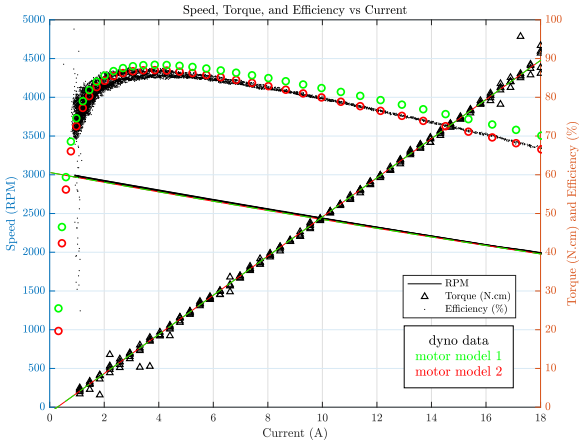


Fig. 5: Motor characterization at 16V and two loss models

A slightly more accurate model can be created by adding one additional term for transmission losses given by $P_t = \alpha_t \tau P_m$, where $\alpha_t$ is an empirical coefficient, $\tau$ denotes torque, and $P_m$ denotes mechanical output power. Efficiency then is given by:

$$\eta_m = 1 - \frac{I^2 R_s + P_Q + P_n(\omega) + \alpha_t \tau P_m}{P_e} \tag{5}$$

which is plotted as "motor model 2" in Figure 5. The authors note that the transmission loss expression was determined purely empirically.

While developing the model, the motor was characterized for 100% duty cycle trapezoidal control at (a) 12V, 14V, 16V, and 18V doing current sweeps and at (b) 2A, 3A, 4A, and 5A doing voltage sweeps. In general, the model was found to have remarkable agreement in all voltage and current levels tested. Figure 5 depicts the measured speed, torque, and efficiency of the motor for the 16V current sweep with the first pass and refined model predictions overlayed. This figure provides a comprehensive description of motor performance and efficiency. Final values of constants used for the models and corresponding datasheet values (where relevant) are provided in Table II. An efficiency map of the motor is produced in Figure 6.

TABLE II: Motor Model Parameters

| Parameter | Datasheet/Nominal Value | Measured/Modelled Value |
|---|---|---|
| $K_v$ | 175 RPM/V | 189 RPM/V |
| $R_s$ | 186mΩ | 249.2mΩ |
| $L_s$ | 0.16mH | 0.28mH |
| $P_Q$ | N/A | 300mW |
| $P_n(\omega)$ | N/A | $\begin{pmatrix} -(7.6\text{e-}12)\text{RPM}^3 \\ +(1.9\text{e-}7)\text{RPM}^2 \\ +(6.7\text{e-}4)\text{RPM} \end{pmatrix}$ W |
| $\alpha_t$ | N/A | 0.006 $(\text{Nm})^{-2}\text{RPM}^{-1}$ |

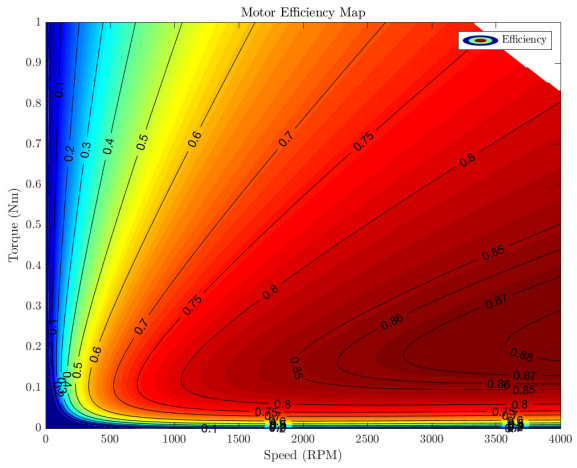


Fig. 6: Modelled efficiency map for the Koford 60LH175 at 16V

## IV. Mechanical Losses

The sources of mechanical losses considered are aerodynamic, tire, wheel, and bearing losses.

### A. Aerodynamic Drag

External aerodynamic drag is the largest loss source in passenger vehicles at highway speeds, accounting for 62.5% of total drag [16]. Great attention was paid to optimize aerodynamics, and Maxwell was uncompromisingly designed for minimum drag. Computational fluid dynamics (CFD) was used heavily in the design, where a single configuration was iterated upon several times to produce a shape with minimum drag while still allowing sufficient space for the driver and powertrain.

Using Altair AcuSolve, the SST turbulence model, and the gamma-Re-theta turbulence transition model, the body of the car was found to have 0.832 N of drag at 15 mph.

However, the exterior of the real vehicle did not match the computer model, as it had surface imperfections and cutouts for the wheels. Both factors increase drag but are very difficult to model in CFD. Because of such discrepancies between simulation and reality, the aerodynamic performance of the real vehicle was verified in a full-scale wind tunnel. It should be noted that the wind tunnel used did not have a moving floor or boundary layer corrections so this test does not fully represent real world conditions. However, Hennig et al. [17] estimate that the error introduced by this does not exceed 3%.

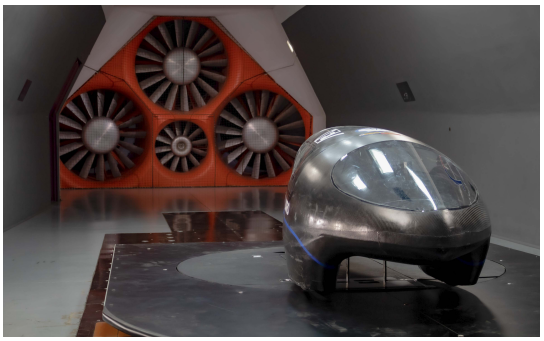

Fig. 7: Maxwell during full-scale wind tunnel tests

The standard model for aerodynamic drag is given by:

$$F_a = \frac{1}{2}\rho v^2 C_d A \tag{6}$$

where $F_a$ is aerodynamic drag force, $\rho$ is the density of air, and $v$ is vehicle speed. Drag area, or $C_dA$, is a single number that combines coefficient of drag and area, allowing direct comparison between vehicles of different sizes. During wind tunnel testing, it was discovered that the vehicle's $C_dA$ was insensitive to airspeed. The $C_dA$ is given in Table III.

TABLE III: Drag Area Estimates

| | $C_dA$ |
|---|---|
| CFD | 0.0308 $m^2$ |
| Wind Tunnel | 0.0438 $m^2$ |

### B. Tire Rolling Resistance

Tire rolling resistance is the force resisting motion of the tire rolling along the road. As the tire rotates, it experiences repeated deformation and recovery. Due to the viscoelastic properties of the rubber, some energy is lost to the hysteresis of the tire [5]. For passenger vehicles, rolling resistance accounts for roughly 37.5% of the total drag on the vehicle at high speeds and roughly 47% in city traffic [16]. For Maxwell and similar supermileage vehicles, rolling resistance accounts for more than one-third of mechanical losses and thus deserves careful treatment.

The retarding force from rolling resistance, $F_{rr}$, can be approximated by:

$$F_{rr} = F_n C_{rr} \tag{7}$$

where $F_n$ is the normal force and $C_{rr}$ is the tire's coefficient of rolling resistance.

A novel eccentric pendulum was constructed to measure rolling resistance. This pendulum, pictured in Figure 8a, is loaded with weights eccentrically so the center of mass is below the axle. When the pendulum is released from non-equilibrium, it will oscillate back and forth in an exponential decay, as in Figure 8b, from which tire characteristics can be determined. The pendulum is instrumented with an inertial measurement unit (IMU) for quantitative analysis. This method of measuring rolling resistance has several advantages compared to the traditional drum test given by [18], as there is no bearing energy loss and minimal aerodynamic and tire misalignment loss.

The initial energy of the system, $E_0$, can be determined by the distance the center of mass is raised above rest, $h$, and the total mass, $m$. The energy lost to rolling resistance, $E_{rr}$, is related to the distance travelled by the contact patch, $d$, found by integrating rotational velocity over time. Conservation of

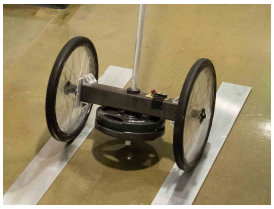

(a)

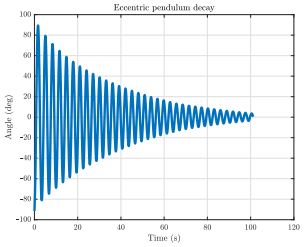


(b)

Fig. 8: (a) Eccentric pendulum used in rolling resistance tests, and (b) measured decay of pendulum oscillations during rolling resistance test

energy implies that after the pendulum has finished oscillating, $E_{rr}$ equals $E_0$. Using this relationship, $C_{rr}$ can be derived using:

$$\begin{aligned} E_0 &= mgh \\ d &= r\int \omega dt \\ E_{rr} &= mgC_{rr}d \\ C_{rr} &= \frac{E_0}{mgd} = \frac{h}{d} \end{aligned} \tag{8}$$

This method was used to determine that the tire used on the car, the Michelin 45/75 R16, has $C_{rr} = 0.0015$ at 7 bar.

### C. Tire Cornering Losses

As the vehicle drives around corners in the track, the tires must produce additional lateral tractive force. To generate this extra force, the tires slip at an angle against the road. The slip angle measures the angle between the tire's forward direction and the actual direction travelled by the vehicle. Slip angle, $\alpha$, and drag force caused by cornering, $F_{cor}$, are given by:

$$\alpha = \frac{mv^2}{rC_a} \tag{9}$$

$$F_{cor} = C_a\alpha^2\frac{\pi}{180} \tag{10}$$

where $r$ is the corner radius and $C_a$ is the tire cornering stiffness parameter. For the Michelin 45/75 R16 in the vehicle, $C_a$ was measured to be 120 N/deg by vehicle coastdown in a circular path.

During the world record attempt, the power loss from cornering peaked at ~35W, approximately double all other mechanical losses combined. As cornering loss force is proportional to $v^4$, optimization of driver velocity and path is critical to achieving peak efficiency.

### D. Wheel Drag: Aerodynamic and Bearing Losses

While the vehicle's wheels are inside the body to avoid disrupting the laminar external airflow, the air inside the car is still affected by the spinning wheels. Additionally, the wheel bearings add further drag to the vehicle. $F_b$, the bearing drag force of a single wheel, and $F_w$, the drag force due to a single wheel's aerodynamics, are given by:

$$F_b = \frac{T_b}{r} \tag{11}$$

$$F_w = \frac{1}{2}\rho v^2 C_d A_w \tag{12}$$

where $C_dA_w$ is the drag area of the faired wheel and $T_b$ is the bearing's frictional moment.

Both were found by the coastdown method on an unloaded wheel and were found to be non-negligible, with $C_dA_w$ measuring $0.0011$ m$^2$ and $T_b$ measuring $4.9$ Nmm. The frictional moment was found to be mostly from bearing seals, and is modelled to be load-independent [19].

## V. Results

In the previous sections, loss models have been formulated for the fuel cell, motor, aerodynamics, rolling resistance, cornering, wheel bearings, and wheel aerodynamics. These loss models can be combined in both a predictive fashion in which the total average efficiency is computed based on nominal race conditions, as well as in a retrospective fashion in which the instantaneous power loss breakdown is estimated for the profile from a historical run. A predictive summary of loss mechanisms is depicted in Figure 9 and a retrospective summary in Figure 10.

### A. Correlation

The ultimate test of applicability for this model is to combine each constituent loss mechanism to predict the performance of the entire vehicle. The difficulty of this task cannot be understated given the plethora of non-idealities, interactions, driver inconsistencies, and other error sources. Despite these challenges, the predictive model estimates a score of 6464 km/l, only a 4.3% deviation from the world record score of 6196 km/l.

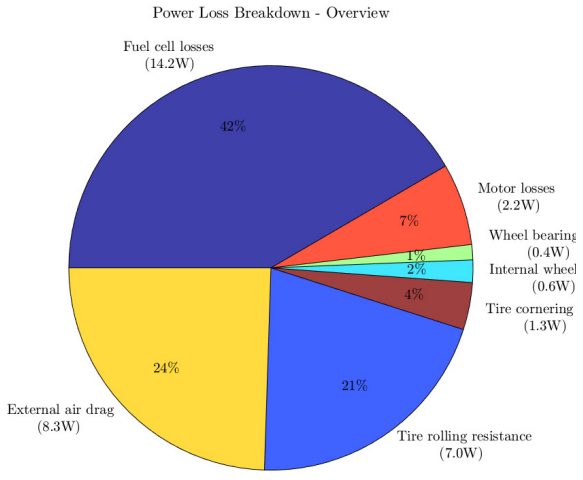


Fig. 9: Average power loss of individual components from the predictive model. Average power from hydrogen flow is 34W.

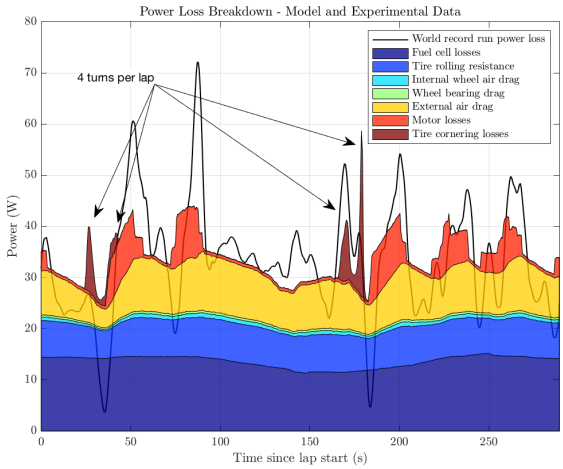


Fig. 10: Instantaneous power loss during the world record run as estimated by constituent models (colored) and by on-board data collection of hydrogen flow compensated for supercapacitor, kinetic, and gravitational potential energies (black).

To further the real-world validation, data logged from the world record run combined with a centimeter-level accurate track map were analyzed to roughly estimate second-by-second power loss. Figure 10 shows a breakdown of the modelled power loss of each mechanism as well as the measured power loss estimated from vehicle sensors. With an integrated error of just 2.6%, the retrospective model has better agreement with the true score than does the predictive model.

### B. Sensitivities

A chief practical application of the models developed in this paper is to perform sensitivity analyses comparing loss mechanisms for efficiency, cost, and time tradeoffs. The symbolic models allow calculation of partial derivatives of loss with respect to any included parameters. They also allow numerical driver strategy simulation and optimization.

Computing optimal driving strategies for supermileage vehicles is an active field of study [20]–[22], but the largest challenge faced is obtaining trustworthy solutions due to lack of accurate models and parameters.

It is the hope of the authors that future works by other vehicle designers utilize the theoretical and empirical models described in this paper to perform their own sensitivity analyses and numerical driver strategy optimizations.

## VI. Conclusion

The analysis of the world record vehicle, Maxwell, consisted of modelling several loss mechanisms. The model for each loss considered was tested in isolation, and the system model resulting from their combination was found to match real world data for both final score as well as instantaneous power loss. This provides strong evidence for the accuracy of all the models developed. These validated component models (reference code available[1]) make a significant contribution to the field of efficient electric and hybrid vehicles by enabling high quality sensitivity analysis and optimization.

## References


[1] US Environmental Protection Agency, "Fuel economy guide, model year 2019," tech. rep., US Department of Energy, 2019.

[2] Shell, "Shell eco-marathon americas 2018 final trophies, prizes and awards," Apr. 2018.

[3] Shell, "Shell eco-marathon americas 2019 official rules chapter ii," Apr. 2019.

[4] Guinness World Records, "Most fuel-efficient vehicle (prototype)." https://www.guinnessworldrecords.com/world-records/most-fuel-efficient-vehicle, 2018.

[5] J. J. Santin, C. H. Onder, J. Bernard, D. Isler, P. Kobler, F. Kolb, N. Weidmann, and L. Guzzella, *The World's Most Fuel Efficient Vehicle: Design and Development of PAC-Car II*. Vdf Hochschulverlag AG an der ETH Zurich, 2007.

[6] T. Hasegawa, H. Imanishi, M. Nada, and Y. Ikogi, "Development of the fuel cell system in the mirai fcv," in *SAE 2016 World Congress and Exhibition*, SAE International, Apr. 2016.

[7] M. Matsunaga, T. Fukushima, and K. Ojima, "Powertrain system of honda fcx clarity fuel cell vehicle," *World Electric Vehicle Journal*, vol. 3, no. 4, pp. 820–829, 2009.

[8] B. K. Hong and S. H. Kim, "Recent advances in fuel cell electric vehicle technologies of hyundai," *ECS Transactions*, vol. 86, no. 13, p. 311, 2018.

[9] T. Matsuura, J. Chen, J. B. Siegel, and A. G. Stefanopoulou, "Degradation phenomena in pem fuel cell with dead-ended anode," *International Journal of Hydrogen Energy*, vol. 38, no. 26, pp. 11346 – 11356, 2013.

[10] M. Piffard, M. Gerard, E. Bideaux, R. D. Fonseca, and P. Massioni, "Control by state observer of pemfc anodic purges in dead-end operating mode," *IFAC-PapersOnLine*, vol. 48, no. 15, pp. 237 – 243, 2015. 4th IFAC Workshop on Engine and Powertrain Control, Simulation and Modeling E-COSM 2015.

[11] H. T. Yap and N. Schofield, "Test characterisation of a h2 pem fuel cell," in *2007 IEEE Vehicle Power and Propulsion Conference*, pp. 551–558, Sep. 2007.

[12] Y. Haseli, "Maximum conversion efficiency of hydrogen fuel cells," *International Journal of Hydrogen Energy*, vol. 43, no. 18, pp. 9015 – 9021, 2018.

[13] S. Mekhilef, R. Saidur, and A. Safari, "Comparative study of different fuel cell technologies," *Renewable and Sustainable Energy Reviews*, vol. 16, no. 1, pp. 981 – 989, 2012.

[14] S. Strahl, A. Husar, and J. Riera, "Experimental study of hydrogen purge effects on performance and efficiency of an open-cathode proton exchange membrane fuel cell system," *Journal of Power Sources*, vol. 248, pp. 474 – 482, 2014.

[15] Koford Engineering LLC, "2.3" (60mm) long length slotless brushless motor 4 pole 24 & 48v windings."

[16] J. Reimpell, H. Stoll, and J. W. Betzler, "2 - tyres and wheels," in *The Automotive Chassis (Second Edition)* (J. Reimpell, H. Stoll, and J. W. Betzler, eds.), pp. 86 – 148, Oxford: Butterworth-Heinemann, second edition ed., 2001.

[17] A. Hennig, N. Widdecke, T. Kuthada, and J. Wiedemann, "Numerical comparison of rolling road systems," Jun. 2011.

[18] SAE Standard J2452, *Stepwise Coastdown Methodology for Measuring Tire Rolling Resistance*, Jul. 2017.

[19] Y. Wang, F. Lin, H. Jiang, and W. Yuan, "Investigation on frictional characteristic of deep-groove ball bearings subjected to radial loads," *Advances in Mechanical Engineering*, vol. 7, no. 7, p. 1687814015586111, 2015.

[20] Guzzella, L., "Modeling and control of advanced propulsion systems," *Oil & Gas Science and Technology - Rev. IFP*, vol. 62, no. 4, pp. 585–594, 2007.

[21] M. Targosz, W. Skarka, and P. Przystałka, "Model-based optimization of velocity strategy for lightweight electric racing cars," *Journal of Advanced Transportation*, vol. 2018, pp. 1–20, Jun. 2018.

[22] N. Filippo, M. Carello, M. D'Auria, and A. Marcello, "Optimization of idrapegasus: Fuel cell hydrogen vehicle," in *SAE 2013 World Congress & Exhibition*, SAE International, Apr. 2013.


[1] https://github.com/DukeElectricVehicles/EnergyLossSim